

Surface structure and stacking of the commensurate $(\sqrt{13} \times \sqrt{13})\mathbf{R}13.9^\circ$ charge density wave phase of $1T\text{-TaS}_2(0001)$

Gevin von Witte,¹ Tilman Kießlinger,² Jan Gerrit Horstmann,¹ Kai Rossnagel,^{3,4,5}
M. Alexander Schneider,² Claus Ropers,¹ and Lutz Hammer^{2,*}

¹*IV. Physical Institute, Georg-August-University Göttingen, D-37077 Göttingen, Germany*

²*Solid State Physics, Friedrich-Alexander-University Erlangen-Nürnberg, D-91058 Erlangen, Germany*

³*Institut für Experimentelle und Angewandte Physik,*

Christian-Albrechts-Universität zu Kiel, D-24098 Kiel, Germany

⁴*Ruprecht-Haensel-Labor, Christian-Albrechts-Universität zu Kiel und Deutsches Elektronen-Synchrotron DESY, D-24098 Kiel und D-22607 Hamburg, Germany*

⁵*Deutsches Elektronen-Synchrotron DESY, D-22607 Hamburg*

By quantitative low-energy electron diffraction (LEED) we investigate the extensively studied commensurate charge density wave (CDW) phase of trigonal tantalum disulphide ($1T\text{-TaS}_2$), which develops at low temperatures with a $(\sqrt{13} \times \sqrt{13})\mathbf{R}13.9^\circ$ periodicity. A full-dynamical analysis of the energy dependence of diffraction spot intensities reveals the entire crystallographic surface structure, i.e. the detailed atomic positions within the outermost two trilayers consisting of 78 atoms as well as the CDW stacking. The analysis is based on an unusually large data set consisting of spectra for 128 inequivalent beams taken in the energy range 20 - 250 eV and an excellent fit quality expressed by a bestfit Pendry R-factor of $R = 0.110$.

The LEED intensity analysis reveals that the well-accepted model of star-of-David-shaped clusters of Ta atoms for the bulk structure also holds for the outermost two TaS_2 trilayers. Specifically, in both layers the clusters of Ta atoms contract laterally by up to 0.25 Å and also slightly rotate within the superstructure cell, causing respective distortions as well as heavy bucklings (up to 0.23 Å) in the adjacent sulphur layers. Most importantly, our analysis finds that the CDWs of the 1st and 2nd trilayer are vertically aligned, while there is a lateral shift of two units of the basic hexagonal lattice (6.71 Å) between the 2nd and 3rd trilayer.

The results may contribute to a better understanding of the intricate electronic structure of the reference compound $1T\text{-TaS}_2$ and guide the way to the analysis of complex structures in similar quantum materials.

PACS numbers: 61.05.jh, 68.35.B-, 71.45.Lr

I. INTRODUCTION

The transition-metal dichalcogenide $1T\text{-TaS}_2$ consists of van der Waals-stacked S-Ta-S trilayers. The $1T$ polytype with octahedrally coordinated Ta atoms exhibits one commensurate $(\sqrt{13} \times \sqrt{13})\mathbf{R}13.9^\circ$ charge-density wave phase (C-phase, $T < 187\text{K}$) and other non-commensurate CDW states at higher temperatures (187K - 543K) [1]. Having been known for decades, these different phases and their transitions [2] are experiencing renewed and growing interest, e.g., following the discovery of pressure-induced superconductivity [3] and optical and electrical switching to metastable “hidden” CDW states [4–8], the observation of ultrafast electronic structure changes at the surface [9–12] and trilayer number-dependent CDW phases in thin crystals [13], as well as the prediction of complex orbital textures [14] and a quantum spin-liquid state associated with the C-phase [15, 16]. Whereas the electronic properties of a single trilayer may often be a good starting point to ex-

plain these various phenomena [17], it has recently become clear that a full understanding of the electronic structure of the CDW states requires to include interlayer coupling and the stacking order of the CDW perpendicular to the trilayers [14]. In the C-phase of $1T\text{-TaS}_2$, for example, different CDW stackings can result in metallic or insulating behavior within the trilayers, but also in a state that corresponds to a band insulator within the trilayers and a metal in the perpendicular direction [18–21]. Thus, detailed knowledge of the three-dimensional atomic and electronic CDW structure is essential, and particularly its modification at the surface as many of the recent key experimental observations were made by surface-sensitive techniques such as scanning tunneling microscopy [5, 7, 8], time- and angle-resolved photoemission spectroscopy [9–12], or ultrafast LEED [2].

Concerning the atomic structure of the CDW phases, Brouwer and Jellinek [22] have taken room-temperature X-ray diffraction (XRD) data for the so-called nearly commensurate (NC) phase, but evaluated them in the approximation of the low-temperature commensurate structure. The true domain structure of the NC-phase has been analyzed in a later XRD study by Yamamoto [23] and refined by Spijkerman et al. [24]. Thus, strictly

* lutz.hammer@fau.de

speaking, for the low-temperature C-phase not even the bulk structure has been precisely determined so far. Only the CDW stacking has been revealed by cross-section transmission electron microscopy, where an alternation of vertical stacking and a particular type of side-shift vectors was found [25]. In this contribution, we investigate the surface structure of this C-phase by a quantitative LEED intensity analysis. The small penetration depth of low-energy electrons yields quantitative structural information for the first and also - with somewhat less accuracy - the second trilayer, which may be taken as representative of the bulk structure.

Recently, Chen and coworkers [26] used quantitative LEED to determine the surface structure of the $1T$ - $\text{TaTe}_2(0001)$ - (3×1) phase, a closely related but less complicated transition metal dichalcogenide phase. Based on a bestfit Pendry R-factor [27] value of $R = 0.29$, they revealed an almost bulk-like structure for the outermost TaTe_2 trilayer. In the present investigation, we will show that a much lower reliability factor value (here $R = 0.11$) is necessary to unambiguously reveal the surface structure of the more complex $(\sqrt{13} \times \sqrt{13})R13.9^\circ$ phase of $1T$ - $\text{TaS}_2(0001)$ and to characterize subtle deviations from the bulk-like structure. Such a fit quality is by no means standard for LEED analyses of systems with such large unit cells. Therefore, this study also intends to provide guidance for the analysis of complex structures through precise data acquisition and consideration of all relevant structural and non-structural parameters in the intensity calculations.

II. LEED EXPERIMENT AND INTENSITY CALCULATIONS

A. LEED experiments

All experiments were performed in a standard ultra-high vacuum (UHV) chamber equipped with all necessary facilities for sample handling, LEED and scanning tunneling microscopy (STM). Details of the apparatus, the sample cleavage and the STM characterization of the surface morphology are given in Appendix A.

The freshly *in-situ* cleaved TaS_2 sample held at about 100 K showed the diffraction pattern of a well-ordered and mono-domain $(\sqrt{13} \times \sqrt{13})R13.9^\circ$ CDW phase, which is displayed for two energies in Fig. 1(a,b). No sign of the second symmetry-equivalent domain rotated by -13.9° against the basic lattice (cf. Fig. 2(a)) could be detected across the whole crystal. Right after cleavage, the TaS_2 surface was aligned in front of the LEED optics for normal incidence of the electron beam via maximum concordance of the intensity vs. energy (voltage) characteristics (IV-spectra) for selected beam triples linked by a 120° rotation (cf. Fig. 1(c,d)). Directly thereafter, a series of images of the complete diffraction pattern was taken as a function of energy (20-250 eV in steps of 0.5 eV) by a highly sensitive CCD camera and stored on

a computer. The whole LEED data acquisition including initial alignment was done within less than one hour after cleavage, i.e., surface contamination can be assumed to be negligible.

Several cycles of heating to ~ 400 K into the IC phase (higher temperatures were incompatible with the adhesive crystal mounting) and subsequent cooling did not lead to any visible changes in the LEED pattern or within the IV spectra. With the conversion into the IC phase, both the local trilayer structure and the CDW stacking are changed completely [1]. Hence the full structural restoration upon cooling, verified by identical LEED-IV spectra, can be taken as a proof that our analysis indeed describes the *equilibrium* surface structure of the C-phase of $1T$ - $\text{TaS}_2(0001)$.

A visual inspection of the LEED patterns in Fig. 1 already suggests a 3-fold symmetry, which becomes even more clearly by comparing IV-spectra for beams being related by a 120° rotation. As shown for two examples in the lower part of the figure all three spectra look rather identical. Of course there are tiny variations in the raw data for the different beams, however, the size of these differences are in the typical range of experimental misalignment in particular of the normal incidence.

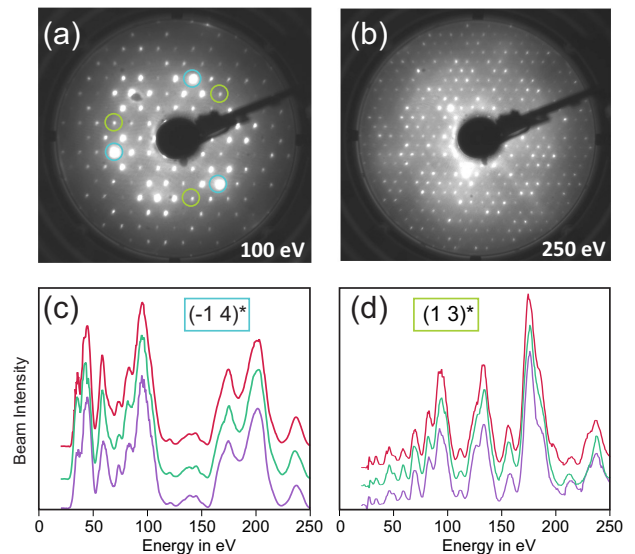


FIG. 1. (Color online) (a,b): LEED pattern of the $(\sqrt{13} \times \sqrt{13})R13.9^\circ$ phase for different energies. (c,d): Comparison of raw experimental IV-spectra for beam triples indicated in the LEED image (a) linked by a 120° rotation. For beam labeling see text.

The stored stack of LEED images made up the raw data base for LEED intensity spectra. In an offline evaluation the IV-spectra for all accessible beams (370 in total) were extracted using the programme package *EE2010* [28], which automatically corrects for the background of the quasi-elastically scattered electrons. This auto-

matic correction requires sufficient space between neighboring diffraction spots to avoid any crosstalk. Thus, the evaluable energy range is limited by the spot density (cf. Fig. 1(b)).

The post-processing of the spectra involved the normalization to the measured, energy-dependent primary beam intensity, averaging over symmetry-related beams, correction for the cosine of the viewing angle as well as noise filtering (7-point median and four times 4th order Savitzky-Golay smoothing over 27 points). This procedure finally resulted in a total data base of 128 symmetrically independent experimental beams for the LEED analysis with a cumulated energy width of $\Delta E = 15383$ eV. The complete set of experimental data used as input for the fitting procedure is provided in the Supplemental Material [29].

B. LEED-IV calculations and error determination

Full-dynamical LEED intensity calculations for selected model configurations were performed using the Erlangen LEED code *TensErLEED* [30]. Starting from these reference structures we conducted an extended fitting procedure using the perturbation method Tensor LEED [31, 32] in combination with a modified random sampling search algorithm [33], both of which are also implemented in the *TensErLEED* program package. After each fitting cycle the resulting bestfit structure was verified by a new full-dynamical intensity calculation, which then served as the reference structure for the next run. Details of the computation are given in Appendix B.

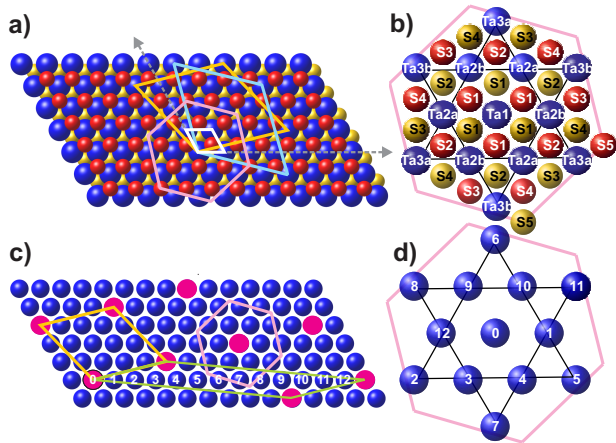


FIG. 2. (Color online) (a) Ball model of a TaS₂ trilayer with the two symmetry equivalent unit meshes of the $(\sqrt{13} \times \sqrt{13})R13.9^\circ$ CDW phase (yellow, cyan) and that of the unreconstructed (1×1) trilayer (white). Also shown in light purple is the hexagonal Wigner-Seitz (WS) cell for the yellow unit cell. (b) Labelling of Ta and S sites within the trilayer WS cell. (c) Alternative CDW unit cell (light green) illustrating the 13 different registry positions, where the central Ta atoms of the next (higher) trilayer can sit. (d) Projection of the registry positions into the WS cell.

In the course of the fit all geometrical parameters of the first (surface) trilayer as well as those of lower lying trilayers (treated as identical) were varied. As outlined in detail in Appendix C, this led to 5 inequivalent Ta and 10 S atoms per trilayer, which are labeled in Fig. 2(b). So, we had to determine the geometrical positions of 30 atoms in total. Adapted to the assumed 3-fold symmetry of the trilayers, the positional deviations were split up in parallel, radial or azimuthal (rotational) displacements with respect to the vertical rotation axis, which led to a total of 78 independent geometrical parameters.

Apart from the local atomic positions within each trilayer also the vertical stacking of the ‘ $\sqrt{13}$ ’-supercells in surface-near trilayers had to be determined as well. In general, there are as many different possible registries as atoms in the unit cell, see Fig. 2(c). Because of the threefold rotational symmetry of the trilayers, the various stackings can be grouped again into 5 classes of symmetrically inequivalent configurations, which are $\{0\}$, $\{1,3,9\}$, $\{4,10,12\}$, $\{2,5,6\}$, and $\{7,8,11\}$ according to the labels given in Fig. 2(d).

Despite the large number of determined structural and non-structural parameters (86 in total) by this analysis, the huge collected database ensures a large redundancy factor of $\varrho = \Delta E / (N \cdot 4V_{0i}) \approx 10$, i.e., we still have ten times more data points than determined parameter values N . The degree of correspondence between calculated and experimental spectra was quantified by the Pendry R-factor R [27], which also allows an estimate of the statistical errors of each parameter via its variance $var(R) = R_{\min} \cdot \sqrt{8 \cdot V_{0i} / \Delta E}$, see Section III B.

III. CRYSTALLOGRAPHIC STRUCTURE OF THE $1T$ -TaS₂($\sqrt{13} \times \sqrt{13}$)R13.9° PHASE

A. Bestfit structural model

The starting point of the whole fitting procedure was the star-of-David-shaped reconstruction model with the parameter set found by Brouwer and Jellinek for their room-temperature approximation of the structure [22]. We interpreted the lateral shifts, mentioned but not further specified in that work, as being entirely radial with respect to the central Ta atom and assumed vertical stacking of the ‘ $\sqrt{13}$ ’-supercells. Without any parameter refinement this structural model produced an only moderate accordance of experimental and calculated data sets expressed by a Pendry R-factor of $R = 0.326$. Such values are only sufficient to exclude any stacking fault in the basic lattice at least within or right below the first trilayer, since those models always led to R-factor values above $R = 0.5$. We refrained from testing fundamentally different structural models but concentrated on the variation of local atomic positions as well as on the superstructure stacking, since the moderate R-factor nevertheless gives some confidence that the star-of-David model also holds for the surface regime, although with local relaxations.

A change of the superstructure stacking implies that the reconstruction pattern of (at least) one trilayer is shifted by one or several basis vectors of the unreconstructed TaS₂ lattice. With such a shift also the assignment of every single atom to certain symmetry-related sites changes (cf. Fig. 2(b)). Hence every stacking sequence has to be treated as a separate structural model for which the whole set of positional parameters has to be adjusted in an independent, complete fit. Since every non-vertical stacking breaks the 3-fold rotational symmetry of the overall system (for a detailed discussion see Appendix C), a domain mixture has to be performed for those models. This means that the IV-spectra of beam triples related by threefold rotation have to be calculated separately and averaged prior to comparison with the experimental data.

In a series of fitting cycles we sequentially investigated all possible models for the CDW stacking of the first and also the second trilayer, which is described in detail in Appendix D. Eventually, we ended up with a bestfit model, where the stacking between 1st and 2nd trilayer is purely vertical (stacking class {0}), while that between 2nd and 3rd trilayer includes a side-shift by two unit vectors of the basic TaS₂ lattice (stacking class {7,8,11}). By that we find exactly the same alternating stacking sequence at the surface as known for the bulk [25], cf. Appendix C. All other stacking models could be excluded on the basis of the Pendry R-factor's variance. The bestfit model is characterized by an ultimate R-factor value of $R = 0.110$, which to our knowledge is the lowest R-factor ever achieved for a LEED-IV analysis of this complexity.

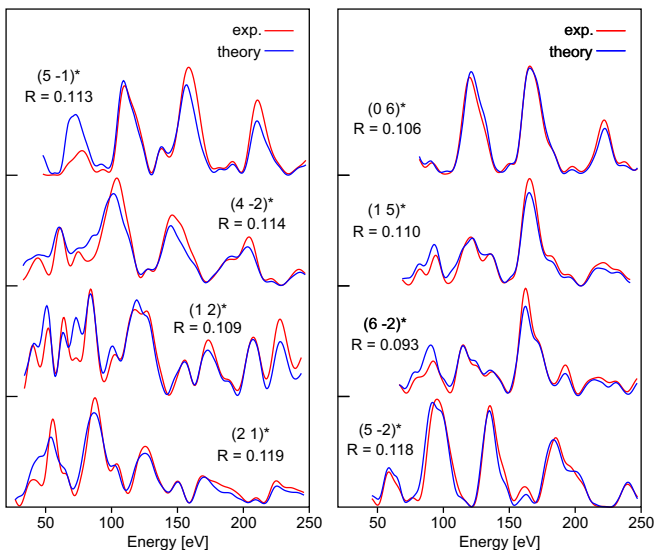


FIG. 3. (Color online) Selection of experimental and bestfit IV-Spectra with single beam R-factors close to the overall R-factor $R = 0.110$ of the analysis. For beam labeling see text.

The fit quality is visualized in Fig. 3 by a selection of experimental and bestfit spectra with single beam R-factors close to the overall R-factor of the analysis. A compilation of the full set of 128 fitted beams is provided

in the Supplemental Material [29]. For better readability, the beams are denoted as multiples of the reciprocal basis vectors of the *supercell mesh*. For differentiation all reciprocal coordinates given according to this superstructure basis are marked by an asterisk. The translation into the usual coordinate system referring to the reciprocal lattice of the unreconstructed TaS₂-crystal is given by $(3\ 1)^* \equiv (1\ 0)$ and $(-1\ 4)^* \equiv (0\ 1)$.

By careful examination of the spectra, it becomes obvious that the fit quality is somewhat deteriorated in the very low energy range below 100 eV. This impression is reinforced by calculating the overall R-factor within small energy intervals. This analysis is displayed in Fig. 4, whereby the statistical weight of the respective intervals (i.e., their share of the total data base) is given by the colour density of the columns. While above 100 eV the bestfit R-factor is even as low as $R = 0.089$ on average, it rises up to about $R = 0.3$ for the lowest energies. Such an energy dependence of the R-factor is frequently observed in particular when heavy atoms (like Ta in our case) are involved and is discussed for the case of Pt by Materer et al. [34]. They interpret this finding as due to the incomplete consideration of spin effects in the LEED computation by just using spin-averaged phase shifts and suggest to ignore intensities below 100 eV in the analysis. Here, we decided to keep the full data basis for completeness.

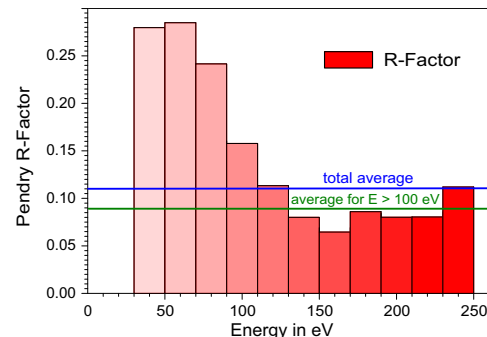


FIG. 4. (Color online) R-factor values calculated within the displayed energy increments of 20 eV width. Also shown is the overall R-factor level and that for energies above 100 eV. The colour density of the columns correspond to the statistical weight of the respective energy range.

The alternate CDW stacking sequence {0} - {7,8,11} revealed by our LEED-IV analysis obviously breaks the 3-fold symmetry of the single trilayers and leaves the surface without any symmetry element (cf. Appendix C). At first glance this seems to be at variance with the experimental finding of a 3-fold symmetric LEED pattern (Fig. 1). With the bestfit IV-spectra at hand, however, we can easily see that for the present structure this symmetry break is indeed very small. Fig. 5 displays various triples of symmetry-related IV-spectra calculated for the bestfit structure. The upper row shows the counterparts to the experimental beams presented in Fig. 1(c,d), while the lower row displays two triples with maximum

mutual spectral differences. Even in these examples the variations were smaller between calculated spectra than towards the experimental ones. The smallness of the effect comes by two different reasons: First, the symmetry break occurs below the 6th layer, i.e., 12 Å deep in the crystal, where the electron wave-field is strongly attenuated. Second, the ascertained registry shift leads to a lateral position in space being rather close to the next rotation axis within the WZ cell, which is at its corner, see Fig. 2(d). Another consequence is that we cannot discriminate from our LEED measurements, whether the determined lateral shift was indeed mono-domain, i.e., either {7}, {8}, or {11}. Alternatively, a domain mixture caused by possible domain boundaries within the CDW or surface steps cannot be ruled out. Accordingly, we cannot ascertain from our experiments, whether the system returns into exactly the same registry after cool-down from the IC-phase or switches between the three alternatives of the {7,8,11} stacking class.

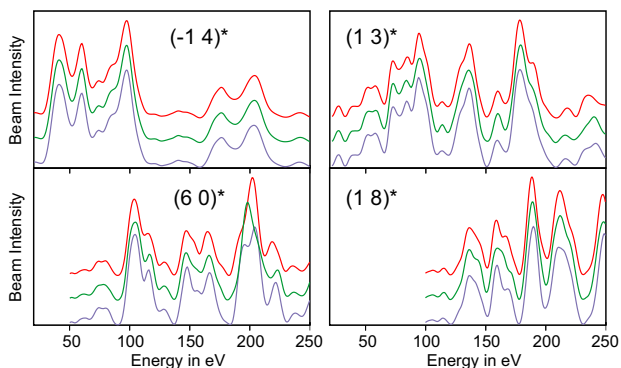


FIG. 5. (Color online) Comparison of calculated spectra for beam triples linked by a 120° rotation.

B. Reliability of the analysis

Before we discuss the atomic structure and possible surface-induced structural variations revealed by the LEED analysis, we first need to know the precision with which the parameter values are determined. A quantitative estimate of error margins is provided by the reliability level of the R-factor $R + var(R)$ [27]: All values for a certain parameter, which lead to a R-factor below this level are assigned to belong to the error margin.

Fig. 6 displays a selection of so-called “error curves”, i.e., the variation of the Pendry R-factor as a function of certain structural parameters like layer distances (top left), vibrational amplitudes (top right) or local displacements of triples of symmetry-related atoms (middle and lower row). A full set of error curves for all 78 fitted structural parameters is provided in the Supplemental Material [29]. The parameter values, at which the error curves intersect the reliability level $R + var(R)$ then represent the related limits in error. As expected, the sensitivity of

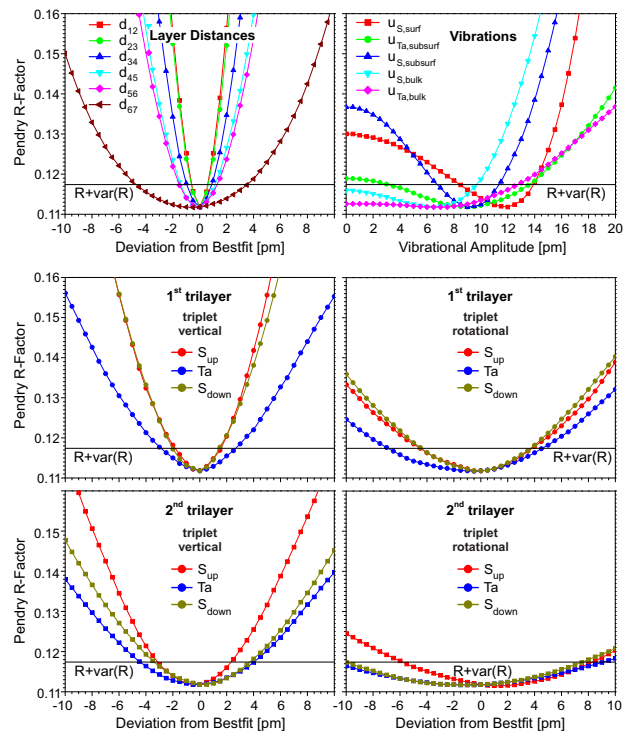


FIG. 6. (Color online) Top row: Error curves for layer distances (left) and vibrational amplitudes (right). Below: Error curves for vertical (left) and rotational lateral displacements (right) of exemplary triples of atoms (S4, Ta2b) within the first (middle row) and second trilayer (bottom row).

the analysis and thus the width of the error bars scales with their depth below the surface (due to attenuation) and inversely with the number of atoms displaced simultaneously. So, layer distances, i.e., the distance of centers of mass of adjacent S or Ta layers, each consisting of 13 atoms, have very small errors. They are below 0.01 Å for the outermost three layer distances, about 0.015 Å for the next two and only then increase to about 0.04 Å below the second trilayer (d_{67}). For vertical displacements of only triples of atoms, which are coupled by the assumed 3-fold rotational symmetry of the trilayers, the error bars are larger, of course. For the first trilayer, they amount to 0.02 Å and 0.03 Å for S and Ta atoms, respectively, and increase to values of about 0.03 Å and 0.045 Å for the second trilayer.

As a general behavior in LEED-IV analyses (performed at normal incidence), the sensitivity towards lateral displacements is reduced by a factor of 2 - 3 compared to vertical ones. This holds also in the present case, where, depending on depth, error margins in the range 0.04 Å - 0.10 Å result.

The size of the error bar only weakly depends on the specific triple of atoms as can be seen by inspection of the Supplemental Material [29]. There is also hardly a difference between radial or rotational lateral displacements. In this sense, the error curves displayed in Fig. 6 can be taken as prototypical. Only the singulets, i.e., the atoms

assuming high symmetry positions within each layer (Ta1 and S5), have 50-100% larger error bars.

Finally, we see in Fig. 6 (top right) that the sensitivity towards vibrational motions is rather low in particular for bulk atoms. Only the outermost S layer exhibits a significantly enlarged vibrational amplitude of 0.12 \AA , while the subsurface Ta and S atoms of the first trilayer show a minimum for $u = 0.09 \text{ \AA}$. The fit of bulk vibration amplitudes leads to numerically even lower values of 0.065 \AA with, however, very little significance, so that the use of common amplitudes for all atoms below the outermost layer would have only spurious effects on the fit quality.

C. Local atomic displacements

Having fixed the superstructure stacking sequence already in Subsection III A, we now want to discuss the bestfit atomic positions within the two outermost trilayers. A rough impression of the scenario can be gained from the ball model displayed in Fig. 7 in top and side view with local CDW-induced displacements magnified by a factor of five. For a more quantitative comparison, the single atomic displacements are visualized in the schematic drawing of Fig. 8 by arrows (lateral) and color-coding (vertical) for every single layer with the respective scalings given in the center. Moreover, the numerical values are all tabulated in Tab. I together with bulk data from literature [22] for comparison.

As expected, we find every 13 Ta atoms of the unit cell clustered in a star-of-David-like formation with mostly radial displacements of the order of 0.2 \AA from their unreconstructed positions (Tab. I and Fig. 8 center row). There are only comparatively small positional differences found for the two Ta layers, though they were completely independently fitted. Also the correspondence to published data for the bulk structure [22] (dashed arrows in Fig. 8) is very close.

As a consequence of the lateral Ta atom clustering, the S atoms bound within the contraction zones (S1, S2) are vertically pushed outwards, and vice versa, they are pulled inwards in the more dilute areas near the edges of the WS cell (S3 - S5), see Figs. 7 and 8. The S atoms also try to follow the Ta atoms laterally, in order to maintain the high symmetric binding configuration. Such a movement, however, is largely restricted ($\leq 0.08 \text{ \AA}$, note the different scaling of the arrows for S and Ta atoms in Fig. 8) by the mutual repulsion of S atoms, which are already rather close packed in the unreconstructed structure. Consequently, the formerly threefold coordination of S atoms towards Ta gets lost with variations in the S-Ta bond lengths by up to 0.2 \AA (in particular for S3 and S4; see also Fig. 7(a)).

From the side view in Fig. 7(b), we also see clearly that there cannot be a strict inversion symmetry between top and bottom S layers (as assumed by Brouwer and Jellinek [22]) due to the alternate stacking sequence, which couples the height modulation of S atoms across the Van-

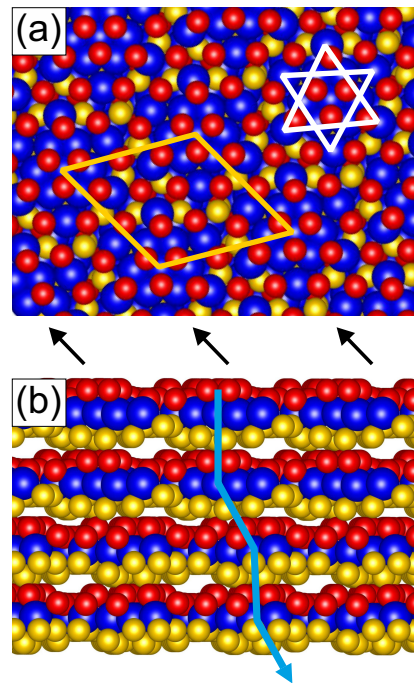


FIG. 7. (Color online) (a) Ball model of the bestfit structure in top view. The atomic displacements from the unreconstructed positions are five times enlarged for better visibility. Also shown are the $(\sqrt{13} \times \sqrt{13})R13.9^\circ$ unit mesh (yellow) and the star-of-David formation of Ta atoms (white). (b) Side view in direction of a superstructure unit vector (indicated by black arrows above) and the stacking sequence of layers (blue).

der-Waals gap either in-phase or (close to) anti-phase. Instead, inversion symmetry should apply for pairs of trilayers, at least in the bulk. As a consequence, slightly alternating layer distances within and between trilayers have to be expected already for the bulk. For the outermost trilayer, this asymmetry might be further enhanced by surface bond relaxations caused by the break of translational symmetry. Indeed, Tab. I reveals slightly different layer distances with the upper S layer always somewhat farther from the center Ta layer than the lower one. While for the second and thus more bulk-like trilayer this difference (0.016 \AA) is within the mutual limits of error, the 0.035 \AA expansion on the outermost S layer compared to d_{23} appears highly significant (error range $\pm 0.006 \text{ \AA}$, c.f. Fig 6 top left). Also an indication for the postulated up-down asymmetry of trilayers is the buckling pattern found for the Ta layers displayed in the center row of Fig. 8. As expected, it is approximately inverse for the two adjacent Ta layers. However, their whole corrugation is too small to be beyond the error margins - a neglectation raises the R-factor in both cases by not more than about 0.002 (a third of the R-factor's variance).

Another interesting finding of our analysis is that the outermost trilayer distance (defined as the mutual distance of the corresponding Ta layers: $c_1 = d_{23} + d_{34} + d_{45} = 5.901 \text{ \AA}$) is smaller by almost 0.02 \AA than

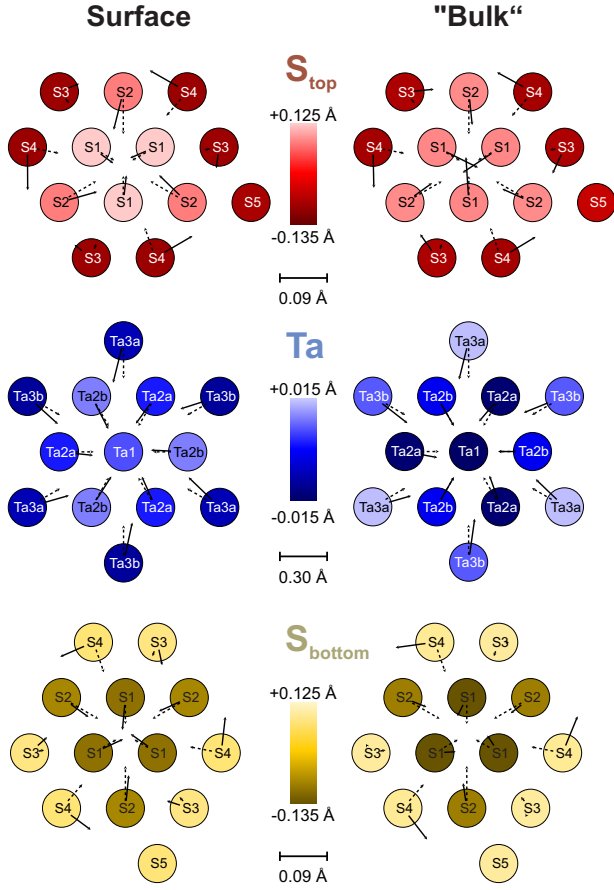


FIG. 8. (Color online) Schematic representation of the CDW-induced layer reconstruction within surface (left) and subsurface (“bulk”) trilayers (right) as derived from the LEED-IV analysis. Vertical displacements are color-coded, size and direction of the lateral ones are indicated by solid arrows (lengths according to the scale bars). Dashed arrows correspond to the XRD analysis of Brouwer and Jellinek [22].

the bulk trilayer distance $c_0 = 5.919 \text{ \AA}$ of the C-phase [35]. Remarkably, this value is very close to the trilayer distance determined for the NC-domain wall structure ($c_0 = 5.896 \text{ \AA}$) [35].

Regarding the lateral displacements, a detailed analysis suffers from the much larger error margins. Therefore, it is advisable to compare mainly the overall patterns displayed in Fig. 8 rather than single atomic coordinates from Tab. I. For both Ta and S layers, we see quite similar patterns in each case with mutual deviations much smaller than the single atomic error margins, which further increases the confidence into the numerical results of this analysis.

For Ta atoms the lateral displacements are mainly radial and caused by the local contraction. However, superimposed there is also an unidirectional azimuthal movement shifting the outer Ta3 atoms with $0.04 \text{ \AA} - 0.06 \text{ \AA}$ about twice as far as the inner Ta2 atoms. In total, this describes a small but concerted rotation of the whole Ta cluster within the $\sqrt{13}$ -supercell. For S atoms, there are

| This work | | | | |
|---|---------------------|---------------|---------------|-----------------|
| Layer | Atom | d_{rad} [Å] | d_{rot} [Å] | d_{\perp} [Å] |
| 1 st trilayer | | | | |
| 1 | S1 | 0.045 | 0.005 | 0.124 |
| | S2 | 0.060 | 0.015 | 0.076 |
| | S3 | 0.010 | -0.030 | -0.086 |
| | S4 | 0.015 | 0.075 | -0.089 |
| | S5 | 0 | 0 | -0.076 |
| layer distance $d_{12} = 1.549 \text{ \AA}$ | | | | |
| 2 | Ta1 | 0 | 0 | 0.006 |
| | Ta2a | 0.199 | 0.020 | 0.002 |
| | Ta2b | 0.219 | 0.010 | 0.009 |
| | Ta3a | 0.245 | 0.061 | -0.008 |
| | Ta3b | 0.235 | 0.051 | -0.005 |
| layer distance $d_{23} = 1.514 \text{ \AA}$ | | | | |
| 3 | S1 | 0.055 | 0.005 | -0.100 |
| | S2 | 0.050 | 0.005 | -0.078 |
| | S3 | 0.025 | -0.015 | 0.080 |
| | S4 | 0.005 | 0.065 | 0.073 |
| | S5 | 0 | 0 | 0.075 |
| layer distance $d_{34} = 2.850 \text{ \AA}$ | | | | |
| 2 nd trilayer | | | | |
| 4 | S1 | 0.080 | -0.005 | 0.083 |
| | S2 | 0.050 | -0.005 | 0.085 |
| | S3 | 0.025 | -0.035 | -0.072 |
| | S4 | 0.015 | 0.070 | -0.080 |
| | S5 | 0 | 0 | -0.050 |
| layer distance $d_{45} = 1.537 \text{ \AA}$ | | | | |
| 5 | Ta1 | 0 | 0 | -0.015 |
| | Ta2a | 0.194 | 0.036 | -0.014 |
| | Ta2b | 0.204 | 0.000 | 0.002 |
| | Ta3a | 0.225 | 0.056 | 0.014 |
| | Ta3b | 0.255 | 0.035 | 0.006 |
| layer distance $d_{56} = 1.521 \text{ \AA}$ | | | | |
| 6 | S1 | 0.030 | 0.015 | -0.134 |
| | S2 | 0.035 | -0.005 | -0.086 |
| | S3 | -0.005 | -0.015 | 0.096 |
| | S4 | -0.015 | 0.075 | 0.091 |
| | S5 | 0 | 0 | 0.096 |
| layer distance $d_{67} = 2.839 \text{ \AA}$ | | | | |
| Brouwer and Jellinek [22] | | | | |
| Atom | d_{\parallel} [Å] | | | d_{\perp} [Å] |
| Ta1 | 0 | | | 0 |
| Ta2 | 0.215 | | | -0.009 |
| Ta3 | 0.236 | | | 0.009 |
| S1 | 0.05 | | | 0.10 |
| S2 | 0.08 | | | 0.05 |
| S3 | 0.01 | | | -0.10 |
| S4 | 0.06 | | | -0.11 |
| S5 | 0 | | | -0.07 |

TABLE I. Atomic displacements from the unreconstructed $1T$ -TaS₂ structure determined by LEED-IV. Lateral movements (d_{\parallel}) are divided into radial (d_{rad}) and rotational components (d_{rot}) w.r.t. the center Ta atom (Ta1) of each trilayer. Layer distances and vertical shifts are given w.r.t. the single layer’s centers of mass with positive sign directing towards the vacuum. For comparison the results of Brouwer and Jellinek [22] for the bulk structure are added below.

even somewhat larger azimuthal displacements though with varying directions. In particular, the sulphur triplet S4 is found to move in all layers almost exclusively rotationally with amplitudes of about 0.07 Å. Most probably, the common rotation is overlaid by local forces caused by the asymmetric binding configurations of S atoms mentioned above. At least the largest rotational displacements of Ta and S atoms within the 1st trilayer are well beyond the error margins, and even for the 2nd trilayer they are still clearly detectable though just within the overall error limit (cf. Fig. 6 center and bottom right). Thus, the rotation of the clusters is indeed a statistically significant property of the CDW-induced structure.

IV. CONCLUSIONS

The full-dynamical LEED-IV analysis presented here provides the first quantitative analysis for the surface and to some extent also for the bulk structure of the low-temperature commensurate CDW phase of 1T-TaS₂. Due to the enormous data basis used for the analysis and the high fit quality achieved, we can determine all atomic positions within the near-surface regime, i.e., for the outermost two trilayers, with the precision of a few picometers. Our analysis reveals that the well-accepted star-of-David-like reconstruction of Ta atoms also holds for the surface with some small surface-specific modifications. In particular, we prove statistically significant an expansion of the outermost S layer and a reduced 1st-2nd trilayer distance. We further find clear evidence that the CDW not only induces a radial contraction of every 13 Ta atoms towards clusters in a ($\sqrt{13} \times \sqrt{13}$)R13.9° periodic arrangement, but also causes a certain common rotation of these clusters within the cell.

The most important and clearest finding of the analysis is that the surface obviously pins a vertical stacking of the CDW-induced ' $\sqrt{13}$ '-supercells between the 1st and 2nd trilayer. The stacking between 2nd and 3rd trilayer, in contrast, turned out to be much more laborious to elucidate and could be resolved with statistical significance only because of the excellent fit quality. It involves a lateral shift of almost half a superstructure unit vector towards one of the equivalent registry positions 7, 8, or 11 according to the labeling of Fig. 2(d). The associated break of 3-fold symmetry is located more than 1 nm below the surface and thus leads to only tiny intensity deviations of symmetry-related spots in the LEED pattern, which are below the detection limit of the present analysis. So, we cannot differentiate here between a real monodomain termination or, alternatively, a domain mixture of extended patches with all three (subsurface) stacking orientations of the {7,8,11} class.

The presented results have two important implications on the surface electronic structure of the low-temperature commensurate CDW phase of 1T-TaS₂. First, it is a remarkable finding that a vertically on-top-stacked double-trilayer is pinned at the surface as this structural unit has

been identified as the driver of CDW stacking-induced energy-gap formation at the Fermi level [14, 19, 21]. Regarding the question about the nature of the ground state of bulk 1T-TaS₂, which density functional theory calculations predict to be a Peierls-type insulator [18, 19, 21], whereas (surface-sensitive) time- and angle-resolved photoemission spectroscopy results indicate dominance of local Mott physics [9–12], this appears to favor the former interpretation. However, it is also possible that the atomic surface structure reported here gives rise to a surface Mott phase. Second, the obtained surface structure clearly reveals a local inversion asymmetry in the surface trilayer due to an asymmetry in the Ta-S layer separations. In principle, the relatively strong spin-orbit coupling in the material can then induce a momentum-dependent spin splitting resulting in spin-polarized surface states [36]. This calls for spin- and angle-resolved photoemission spectroscopy measurements. The detailed atomic surface structure thus emerges as an important ingredient in any understanding of the intriguing electronic phenomena probed by surface-sensitive techniques [2, 5, 7–12, 19, 20]. There is clearly a need for further theoretical and experimental scrutiny of the atomic and electronic surface structure of 1T-TaS₂ and related materials, both for bulk and few-trilayer crystals.

This work was supported by the European Research Council (ERC StG, ID: 639119).

Appendix A: Experimental details

The TaS₂ sample (diameter about 3 mm, thickness 0.5 mm) was grown as described in the supplement of Ref. 12. Here, it was mounted on a copper support plate at the sample transfer holder using an electrically conducting two-component adhesive. At the top of the sample a ceramic stick was fixed with the same adhesive. The transfer holder was then introduced into the UHV ($p < 2 \cdot 10^{-10}$ mbar) chamber via a two-stage load-lock system and mounted on the manipulator, which allowed for high-precision x-, y-, z-translations, rotation around an axis within the sample's surface and tilt against its normal. The sample was cooled by direct contact to a liquid nitrogen reservoir and heated either by a hot filament or by additional electron bombardment from the rear, whereby the temperature was monitored using a K-type thermocouple attached to the Cu base plate. After careful degassing of the sample holder, the TaS₂ crystal was cooled down to about 100 K and subsequently cleaved by hitting the ceramic stick glued on the crystal with a wobble-stick. In order to avoid any time loss prior to the LEED experiment the cleavage was performed right in front of the LEED optics.

After completion of all LEED experiments described in Subsection II A (≈ 1 day after cleavage) the sample was transferred to a room-temperature STM within the same UHV apparatus for further characterization of the

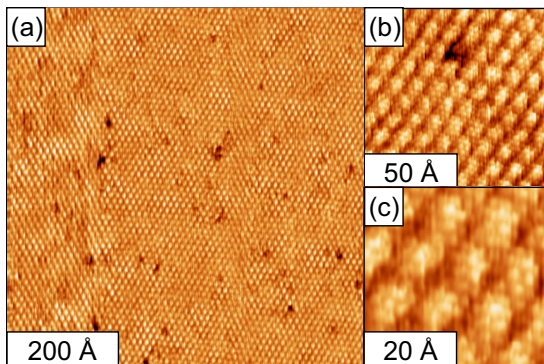


FIG. 9. (Color online) (a) Room-temperature STM survey image of the TaS₂ sample taken 30 h after cleavage ($U_{\text{sample}} = -90$ mV; $I = 1.3$ nA). (b,c) Same as (a) but with atomic resolution. ($U_{\text{sample}} = +5$ mV; $I = 3.4$ nA).

surface morphology. Unfortunately, at room temperature the C-phase is no more stable, so that only the NC-phase could be imaged here. Large-scale STM topographs (Fig. 9(a)) were taken at different places of the sample. These always showed the pseudo-regular arrangement of ‘ $\sqrt{13}$ ’-unit cells with spatially varying contrast typical for the long-range domain structure of the NC-phase [37–39]. The moiré-type atomic configuration of topmost sulphur atoms can directly be seen in the atomically resolved picture displayed in Fig. 9(b). STM also reveals a small density of randomly distributed defects imaged as depressions with an apparent depth of about 2 Å and typical sizes of the order of whole ‘ $\sqrt{13}$ ’-unit cells. Since clusters of missing sulphur atoms seem rather improbable, we tentatively attribute these depressions to spurious contaminations adsorbed during the one day exposure to the residual gas atmosphere of the UHV chamber. Remarkably, we did not find any single atomic step during the entire STM investigation performed at various places across the crystal’s surface.

Appendix B: Computational details

Phase shifts were calculated by J. Rundgren’s program *EEASiSSS* [40] for an unreconstructed 1T-TaS₂ crystal. Due to the comparably low maximum energy of 250 eV, values of $\ell_{\text{max}} = 9$ turned out to be sufficient. This program also calculates self-consistently the corresponding dependence of the real part of the inner potential on the electron energy E : $V_{0r} = \max[(-0.05 - 63.42/\sqrt{E + 17.15}, -9.00)$ eV. To account for the filament’s work function and calibration uncertainties a constant offset V_{00} for the electron energy was adjusted within the analysis resulting in a value of $V_{00} = -3.0$ eV. The damping of the electrons due to inelastic processes was considered by a constant optical potential V_{0i} , which was fitted to 4.75 eV in a later stage of the analysis. As lateral lattice parameter we used $a_{\text{TaS}_2} = 3.354$ Å, which was extrapolated from the temperature dependence given

in Ref. 35 to our data acquisition temperature of 100 K. A vertical lattice parameter c was not introduced to the calculations but resulted automatically from the fit of individual layer distances.

For better convergence of the fit, vertical, parallel, and rotational displacements were optimized separately in an iterative process, whereby the grid widths were successively reduced down to 0.0025 Å for vertical and 0.005 Å for lateral parameters, since for the latter, normal incidence LEED is less sensitive. The iterations converged rapidly, indicating that parameter dependencies between the different parameter classes are quite small. Additionally, the (common) vibrational amplitude of the surface S atoms was adjusted, while the vibrations of bulk atoms were first kept fixed at values derived from Ref. 24. Finally, and only for the bestfit configuration, the vibrational amplitudes (taken as isotropic) of all three layers of the topmost trilayer as well as for bulk Ta and S atoms were optimized without readjusting the geometrical parameters. Also, the angular spread within the slightly convergent primary beam used in the LEED experiment was accounted for by a small off-normal angle of incidence (here fitted to 0.51°) and averaging over 6 azimuthal directions of incidence ($\Phi = 0^\circ, 60^\circ, \dots$).

The parameter variations for error determination were performed in the TensorLEED approximation and as usual with all other parameters held fixed at their best-fit value. This procedure saves enormous computational time, but as a drawback it neglects possible parameter correlations. Experience tells that such correlations increasingly diminish with the size of the data base used for the analysis, which is with more than 15 keV quite huge in our case. Moreover, in the course of fitting we did not find any hint for significant parameter coupling, so that we have confidence in our error estimate. We also note that, again for sake of computational time minimization, the R-factor calculation was not performed for the azimuthally averaged spectra but for one single azimuth of incidence ($\Phi = 0^\circ$) only. For this setup the minimum R-factor was slightly higher ($R = 0.112$) and so also the reliability level $R + \text{var}(R) = 0.118$. This, however, means in effect just a practically rigid upward shift of the curves by $\Delta R = 0.002$ with no measurable consequences for the error bar determination.

Appendix C: Trilayer symmetry and CDW stacking

A prerequisite for any LEED-IV structure determination is a proper analysis of the symmetry of considered structural models, in order to identify symmetry-related groupings of atoms and parameter constraints. It should be noted that the mere existence of the surface only allows for surface-normal mirror or glide planes as well as rotation axes.

The unreconstructed 1T-TaS₂ structure consists of primitive hexagonal sulphur or tantalum layers. They are packed to S-Ta-S trilayers with an internal fcc-like

A–B–C layer stacking, which reduces the p6m symmetry of the single layers to p3m. With the formation of the CDW-induced ($\sqrt{13} \times \sqrt{13}$) reconstruction with 13.9° rotational angle any mirror plane gets lost, independent of the detailed nature of the distortion. Therefore, the new supercell has at maximum a 3-fold rotational symmetry (p3). Consequently, two symmetrically equivalent superstructure domains are possible (both displayed in Fig. 2(a)) being rotated by either $+13.9^\circ$ or -13.9° with respect to the unit mesh of the basic (unreconstructed) lattice.

The Wigner-Seitz (WS) cell of the ' $\sqrt{13}$ '-superstructure contains 39 atoms per trilayer - 13 Ta- and 26 S-atoms - as shown in Fig. 2(b). Rotation axes intersect the WS cell in the center and the corners, thus in each single Ta- or S-layer there is just one atom of the WS cell on a rotation axis. All other atoms must be grouped into triples linked by the 3-fold rotational symmetry. In total, there are 5 symmetrically inequivalent atomic sites per single S or Ta layer (15 per trilayer) labeled in Fig. 2(b). This labeling of sites is adopted from Brouwer and Jellinek [22], who, however, treated the Ta layer (inaccurately) as sixfold symmetric. Hence, we use extra labels “a” and “b” for discrimination.

In unreconstructed 1T-TaS₂ the trilayers are stacked vertically on top of each other. Any CDW-induced reconstruction is not expected to lead to a change of this principal layer stacking, since that would require a concerted movement of entire S or Ta layers. Nevertheless, such stacking faults have occasionally been observed by scanning transmission electron microscopy in exfoliated 1T-TaS₂ samples [41]. Therefore, it cannot be excluded *a priori* that such a stacking fault might be induced near the very surface by the cleavage process, an additional option, which has to be regarded in the fitting process. A completely different question, however, is the stacking of the ' $\sqrt{13}$ '-supercells, i.e., whether there is a lateral phase shift between CDWs of adjacent trilayers. In total, there are 13 different possible registries, which can easily be visualized by choosing the alternative representation of the translational unit cell shown in Fig. 2(c) (light green rhomb). A back-projection of these registries into the WS cell is displayed in Fig. 2(d). Obviously, any registry except the vertical stacking {0} breaks the 3-fold rotational symmetry of the single trilayer and leaves the surface model without any remaining symmetry element (p1).

The internal 3-fold rotational symmetry of each trilayer, however, will hardly be affected by the symmetry break across the Van-der-Waals gap. Thus, the various stackings can be grouped again into 5 classes of symmetrically inequivalent configurations, which are {0}, {1,3,9}, {4,10,12}, {2,5,6}, and {7,8,11} according to the labels given in Fig. 2(d). While the supercell stacking in the commensurate CDW phase of 1T-TaS₂ could not be unequivocally resolved by X-ray [42] or electron diffraction studies [43], it was revealed by transmission electron microscopy [25] as alternating between the classes {0}

and {7,8,11}. In their study, Ishiguro and Sato [25] found that with very few exceptions, every vertical stacking is followed by another with lateral shift, whereby both alternatives, i.e., “sliding” (e.g., 0,8,0,8,0,8,...) as well as “screw” stacking (e.g., 0,7,0,8,0,11,...), occurred locally indicating a partially disordered vertical stacking.

Appendix D: Fitting procedure and model discrimination

In order to save some computational time we performed the rough model exclusion with a reduced data set consisting of 66 beams only, which is about half of the total data base. In a first round, we investigated models with different superstructure stackings between the first and second trilayer and - for simplicity - vertical stacking below. We sequentially adjusted vertical and radial displacements of atoms within each model, disregarding any rotational degree of freedom. It turned out that a vertical superstructure stacking between the outermost two trilayers resulted in a much lower R-factor value of $R = 0.191$ compared to values of $R = 0.270 - 0.338$ for the four other stacking classes, cf. upper part of Table II. At that stage of fitting, the variance of the current best R-factor was already as low as $var(R) = 0.013$, i.e., all models with R-factor values way above $R + var(R) = 0.204$ can safely be excluded.

| 1 st - 2 nd trilayer stacking | | | | | |
|---|--------------|---------|-----------|---------|-----------------|
| Stacking class | {0} | {1,3,9} | {4,10,12} | {2,5,6} | {7,8,11} |
| R-factor | 0.191 | 0.284 | 0.306 | 0.270 | 0.338 |
| 2 nd - 3 rd trilayer stacking | | | | | |
| Stacking class | {0} | {1,3,9} | {4,10,12} | {2,5,6} | {7,8,11} |
| R-factor | 0.160 | 0.166 | 0.154 | 0.143 | 0.139 |
| R(fine-grid) | — | — | — | 0.132 | 0.125 |
| R(all data) | — | — | — | 0.131 | 0.123 |
| R(angular corr.) | — | — | — | — | 0.113 |
| R(vibr. opt.) | — | — | — | — | 0.110 |

TABLE II. Pendry R-factor values achieved for different models of superstructure stacking and stages of fit refining. For details see text.

Next, we compared all different stacking models for the 2nd to 3rd trilayer positioning while keeping the superstructure stacking of the outermost trilayer fixed at the vertical class {0}. Note that all these models have the outermost six S or Ta layers in common, i.e., they start to differ from each other only at a depth of about 12 Å, where the electron wave-field has already been greatly attenuated by inelastic scattering. Hence, the R-factor differences between different models will be much smaller. Therefore, the fit was performed at a more elaborate level by additionally regarding rotational atomic movements with respect to the central Ta atom. This reduced

the overall R-factor level, e.g., $R = 0.191 \rightarrow 0.160$ for the “all-vertical” model. As can be seen in the lower part of Table II, there are still significant differences in the R-factor values for the various models. The bestfit ($R = 0.139$) is achieved for a {7,8,11} stacking. However, also a {2,5,6} stacking would be consistent with the data, given the variance of the R-factor at this fit level ($\text{var}(R) = 0.0095$). All other stackings can already be excluded.

For these two remaining models, we then performed the structural search on a finer grid (0.005 Å for lateral and 0.0025 Å for vertical displacements) around the respective former bestfit configurations, which brought both R-factor values further down and also increased their relative distance, though still not beyond the variance level. This, however, could be reduced by increasing the data basis of the fit. With the whole available data of more than 15 keV in total, the models finally differed by $\Delta R = 0.008$, while the variance, scaling inversely with

the square root of the data base size, became as low as $\text{var}(R) = 0.006$.

Although the R-factor variance level is by no means a sharp limit for the unambiguous exclusion of a model we have strong confidence that the {7,8,11} class is indeed the correct description for the 2nd to 3rd trilayer stacking. This is backed by the observation that the bestfit for the {2,5,6} model produced physically rather implausible atomic displacements in parts, which did not occur for the {7,8,11} class. Finally, it is also quite striking that we just find the very same stacking sequence at the surface as known for the bulk [25], cf. Appendix C.

For further reducing the R-factor value of the bestfit model - and with that the error margins of the analysis - we eventually corrected the intensity calculations for effects of the slightly convergent beam of incoming electrons and optimized the vibrational amplitudes of surface and bulk S and Ta atoms.

-
- [1] C. B. Scruby, P. M. Williams, and G. S. Parry, *The Philosophical Magazine: A Journal of Theoretical Experimental and Applied Physics* **31**, 255 (1975).
- [2] S. Vogelgesang, G. Storeck, J. G. Horstmann, T. Diekmann, M. Sivis, S. Schramm, K. Rossnagel, S. Schäfer, and C. Ropers, *Nature Physics* **14**, 184 (2018).
- [3] B. Sipos, A. F. Kusmartseva, A. Akrap, H. Berger, L. Forró, and E. Tutiš, *Nature Materials* **7**, 960 (2008).
- [4] L. Stojchevska, I. Vaskivskiy, T. Mertelj, P. Kusar, D. Svetin, S. Brazovskii, and D. Mihailovic, *Science* **344**, 177 (2014).
- [5] D. Cho, S. Cheon, K.-S. Kim, S.-H. Lee, Y.-H. Cho, S.-W. Cheong, and H. W. Yeom, *Nature Communications* **7**, 10453 (2016).
- [6] I. Vaskivskiy, I. A. Mihailovic, S. Brazovskii, J. Gospodaric, T. Mertelj, D. Svetin, P. Sutar, and D. Mihailovic, *Nature Communications* **7**, 11442 (2016).
- [7] L. Ma, C. Ye, Y. Yu, X. F. Lu, X. Niu, S. Kim, D. Feng, D. Tománek, Y.-W. Son, X. H. Chen, and Y. Zhang, *Nature Communications* **7**, 10956 (2016).
- [8] Y. A. Gerasimenko, P. Karpov, I. Vaskivskiy, S. Brazovskii, and D. Mihailovic, *npj Quantum Materials* **32**, 4 (2019).
- [9] L. Perfetti, P. A. Loukakos, M. Lisowski, U. Bovensiepen, H. Berger, S. Biermann, P. S. Cornaglia, A. Georges, and M. Wolf, *Phys. Rev. Lett.* **97**, 067402 (2006).
- [10] J. C. Petersen, S. Kaiser, N. Dean, A. Simoncig, H. Y. Liu, A. L. Cavalieri, C. Cacho, I. C. E. Turcu, E. Springate, F. Frassetto, L. Poletto, S. S. Dhesi, H. Berger, and A. Cavalleri, *Phys. Rev. Lett.* **107**, 177402 (2011).
- [11] S. Hellmann, T. Rohwer, M. Källäne, K. Hanff, C. Sohrt, A. Stange, A. Carr, M. Murnane, H. Kapteyn, L. Kipp, M. Bauer, and K. Rossnagel, *Nature Communications* **3**, 1069 (2012).
- [12] M. Ligges, I. Avigo, D. Golež, H. U. R. Strand, Y. Beyazit, K. Hanff, F. Diekmann, L. Stojchevska, M. Källäne, P. Zhou, K. Rossnagel, M. Eckstein, P. Werner, and U. Bovensiepen, *Phys. Rev. Lett.* **120**, 166401 (2018).
- [13] Y. Yu, F. Yang, X. F. Lu, Y. J. Yan, Y.-H. Cho, L. Ma, X. Niu, S. Kim, Y.-W. Son, D. Feng, S. Li, S.-W. Cheong, X. H. Chen, and Y. Zhang, *Nature Nanotechnology* **10**, 270 (2015).
- [14] T. Ritschel, J. Trinckauf, K. Koepf, B. Büchner, M. V. Zimmermann, H. Berger, Y. I. Joe, P. Abbamonte, and J. Geck, *Nature Physics* **11**, 328 (2015).
- [15] K. T. Law and P. A. Lee, *Proceedings of the National Academy of Sciences* **114**, 6996 (2017).
- [16] M. Klanjšek, A. Zorko, R. Žitko, J. Mravlje, Z. Jagličić, P. Biswas, P. Prelovšek, D. Mihailovic, and D. Arčon, *Nature Physics* **13**, 1130 (2017).
- [17] K. Rossnagel and N. V. Smith, *Phys. Rev. B* **73**, 073106 (2006).
- [18] P. Darancet, A. J. Millis, and C. A. Marianetti, *Phys. Rev. B* **90**, 045134 (2014).
- [19] T. Ritschel, H. Berger, and J. Geck, *Phys. Rev. B* **98**, 195134 (2018).
- [20] A. S. Ngankeu, S. K. Mahatha, K. Guilloy, M. Bianchi, C. E. Sanders, K. Hanff, K. Rossnagel, J. A. Miwa, C. Breth Nielsen, M. Bremholm, and P. Hofmann, *Phys. Rev. B* **96**, 195147 (2017).
- [21] S.-H. Lee, J. S. Goh, and D. Cho, *Phys. Rev. Lett.* **122**, 106404 (2019).
- [22] R. Brouwer and F. Jellinek, *Physica B* **99**, 51 (1980).
- [23] A. Yamamoto, *Phys. Rev. B* **27**, 7823 (1983).
- [24] A. Spijkerman, J. L. de Boer, A. Meetsma, G. A. Wieggers, and S. van Smaalen, *Phys. Rev. B* **56**, 13757 (1997).
- [25] T. Ishiguro and H. Sato, *Phys. Rev. B* **44**, 2046 (1991).
- [26] C. Chen, H.-S. Kim, A. S. Admasu, S.-W. Cheong, K. Haule, D. Vanderbilt, and W. Wu, *Phys. Rev. B* **98**, 195423 (2018).
- [27] J. B. Pendry, *Journal of Physics C: Solid State Physics* **13**, 937 (1980).
- [28] M. F. Opheys, <http://www.ee2000.de> (2011).
- [29] See Supplemental Material at [URL] for tabulated coordinates of the bestfit structure as well as graphs comprising

a comparison of experimental and best-fit LEED-IV spectra and “error curves” (R-factor vs deviation from bestfit value) for all fitted structural parameters. Also a file with experimental intensity-vs-energy data is provided.

- [30] V. Blum and K. Heinz, *Computer Physics Communications* **134**, 392 (2001).
- [31] K. Heinz, *Rep. Prog. Phys.* **58**, 637 (1995).
- [32] P. J. Rous, J. B. Pendry, D. K. Saldin, K. Heinz, K. Müller, and N. Bickel, *Phys. Rev. Lett.* **57**, 2951 (1986).
- [33] M. Kottcke and K. Heinz, *Surface Science* **376**, 352 (1997).
- [34] N. Materer, U. Starke, A. Barbieri, R. Döll, K. Heinz, M. V. Hove, and G. Somorjai, *Surface Science* **325**, 207 (1995).
- [35] F. Givens and G. Fredericks, *Journal of Physics and Chemistry of Solids* **38**, 1363 (1977).
- [36] J. M. Riley, F. Mazzola, M. Dendzik, M. Michiardi, T. Takayama, L. Bawden, C. Granerod, M. Leandersson, T. Balasubramanian, M. Hoesch, T. K. Kim, H. Takagi, W. Meevasana, P. Hofmann, M. Bahramy, J. Wells, and P. D. C. King, *Nature Physics* **10**, 835 (2014).
- [37] B. Burk, R. E. Thomson, A. Zettl, and J. Clarke, *Phys. Rev. Lett.* **66**, 3040 (1991).
- [38] R. E. Thomson, B. Burk, A. Zettl, and J. Clarke, *Phys. Rev. B* **49**, 16899 (1994).
- [39] H. Bando, Y. Miyahara, H. Enomoto, and H. Ozaki, *Surface Science* **381**, L609 (1997).
- [40] J. Rundgren, *Phys. Rev. B* **68**, 125405 (2003).
- [41] R. Hovden, A. W. Tsen, P. Liu, B. H. Savitzky, I. El Baggari, Y. Liu, W. Lu, Y. Sun, P. Kim, A. N. Pasupathy, and L. F. Kourkoutis, *Proceedings of the National Academy of Sciences* **113**, 11420 (2016), <https://www.pnas.org/content/113/41/11420.full.pdf>.
- [42] S. Tanda, T. Sambongi, T. Tani, and S. Tanaka, *J. Phys. Soc. Jpn.* **53**, 476 (1984).
- [43] K. Fung, J. Steeds, and J. Eades, *Physica B+C* **99**, 47 (1980).

SUPPLEMENTARY INFORMATION

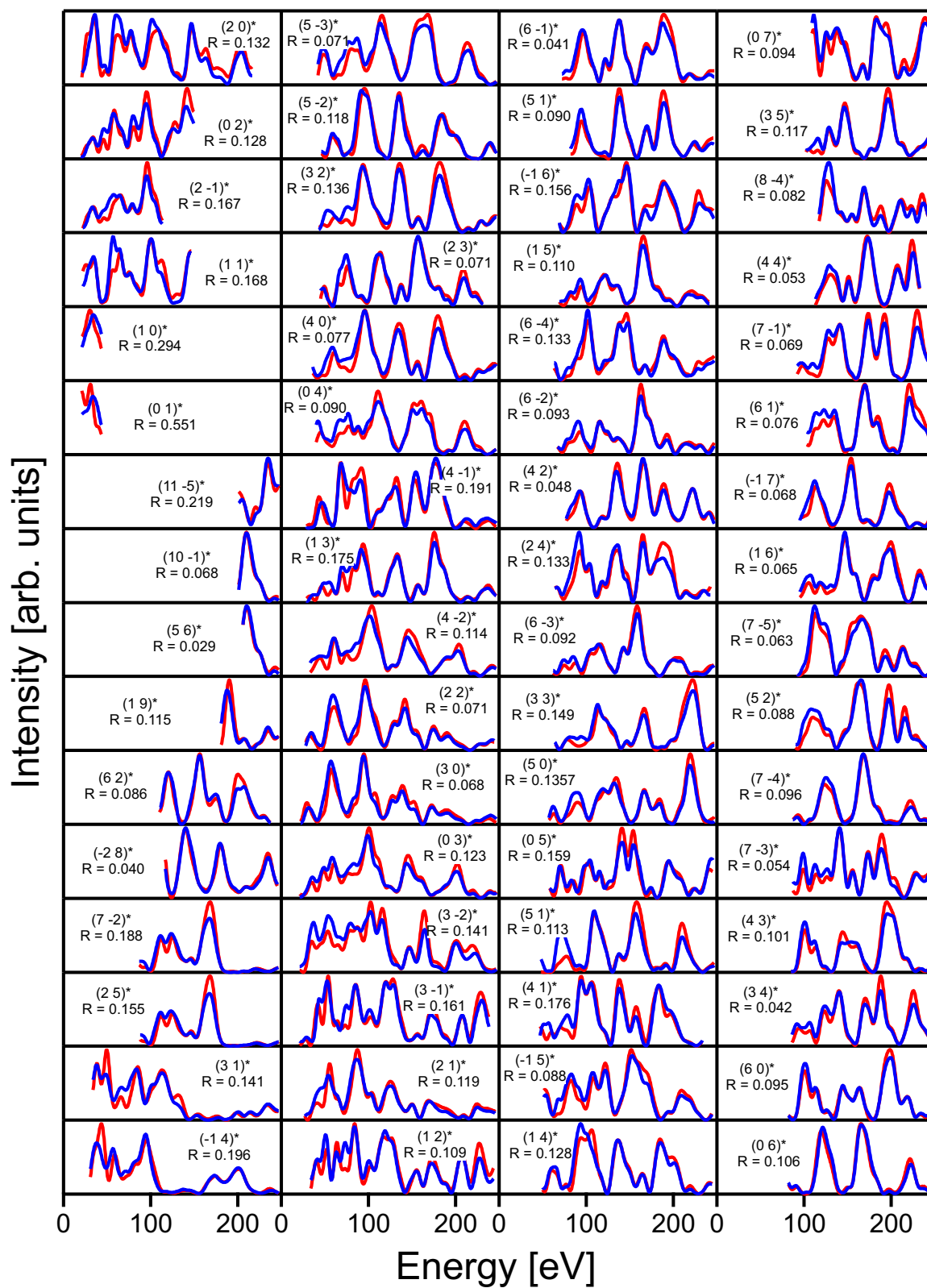
This supplement comprises tabulated coordinates of the the bestfit structure as well as plots of all experimental and calculated bestfit spectra and “error curves” for all fitted atomic displacements.

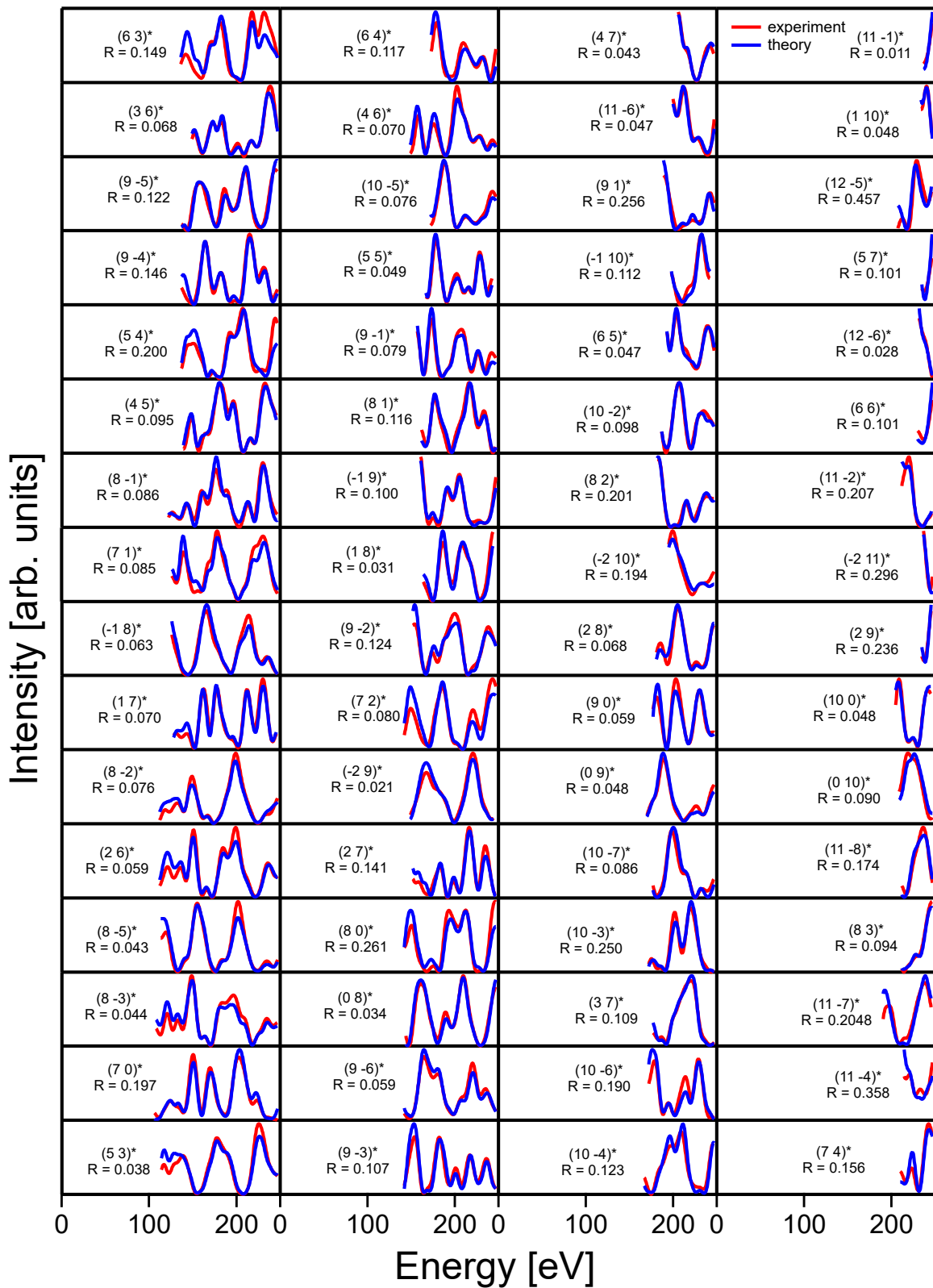
ATOMIC COORDINATES OF THE LEED BESTFIT STRUCTURE

| Atom | X [Å] | Y [Å] | Z [Å] | Atom | X [Å] | Y [Å] | Z [Å] |
|-------|---------|---------|--------|-------|---------|---------|--------|
| S11 | 1.6355 | 0.9500 | 0.0000 | S41 | 1.6101 | 0.9238 | 5.9525 |
| S14 | 3.2871 | 3.9100 | 0.2125 | S44 | 3.2909 | 3.9067 | 6.1150 |
| S13 | 5.0264 | 0.9370 | 0.2100 | S43 | 5.0125 | 0.9291 | 6.1075 |
| S12 | 3.3096 | -1.8935 | 0.0475 | S42 | 3.3080 | -1.9156 | 5.9500 |
| S11 | 0.0050 | -1.8914 | 0.0000 | S41 | -0.0050 | -1.8565 | 5.9525 |
| S11 | -1.6405 | 0.9415 | 0.0000 | S41 | -1.6051 | 0.9325 | 5.9525 |
| S12 | -0.0150 | 3.8129 | 0.0475 | S42 | 0.0050 | 3.8228 | 5.9500 |
| S13 | 1.6355 | -4.8216 | 0.2100 | S43 | -1.7016 | -4.8055 | 6.1075 |
| S14 | -5.0298 | 0.8918 | 0.2125 | S44 | -5.0288 | 0.8968 | 6.1150 |
| S15 | 6.7076 | -1.9363 | 0.2000 | S45 | 6.7076 | -1.9363 | 6.0850 |
| S14 | 1.7425 | -4.8015 | 0.2125 | S44 | 1.7379 | -4.8034 | 6.1150 |
| S12 | -3.2946 | -1.9194 | 0.0475 | S42 | -3.3129 | -1.9070 | 5.9500 |
| S13 | -3.3246 | 3.8846 | 0.2100 | S43 | -3.3110 | 3.8763 | 6.1075 |
| Ta21 | 0.0000 | 0.0000 | 1.6675 | Ta51 | 0.0000 | 0.0000 | 7.5875 |
| Ta22a | 1.5600 | 2.7417 | 1.6715 | Ta52a | 1.5495 | 2.7533 | 7.5865 |
| Ta22b | 3.1345 | 0.0100 | 1.6640 | Ta52b | 3.1494 | 0.0000 | 7.5740 |
| Ta22a | 1.5945 | -2.7218 | 1.6715 | Ta52a | 1.6097 | -2.7185 | 7.5865 |
| Ta22b | -1.5586 | -2.7195 | 1.6640 | Ta52b | -1.5748 | -2.7274 | 7.5740 |
| Ta22a | -3.1543 | -0.0199 | 1.6715 | Ta52a | -3.1591 | -0.0349 | 7.5865 |
| Ta22 | -1.5760 | 2.7095 | 1.6640 | Ta52b | -1.5747 | 2.7275 | 7.5740 |
| Ta23a | -0.0598 | 5.5635 | 1.6810 | Ta53a | -0.0548 | 5.5833 | 7.5585 |
| Ta23b | 4.8022 | 2.8301 | 1.6785 | Ta53b | 4.7923 | 2.8069 | 7.5660 |
| Ta23a | 4.8480 | -2.7299 | 1.6810 | Ta53a | 4.8626 | -2.7442 | 7.5585 |
| Ta23b | 0.0499 | -5.5737 | 1.6785 | Ta53b | 0.0348 | -5.5536 | 7.5660 |
| Ta23a | -4.7882 | -2.8336 | 1.6810 | Ta53a | -4.8078 | -2.8392 | 7.5585 |
| Ta23b | -4.8521 | 2.7437 | 1.6785 | Ta53b | -4.8271 | 2.7467 | 7.5660 |
| S31 | 1.6318 | -0.9364 | 3.2855 | S61 | 1.6584 | -0.9402 | 9.2275 |
| S32 | 3.3082 | 1.9157 | 3.2630 | S62 | 3.3260 | 1.9146 | 9.1800 |
| S34 | 5.0376 | -0.9034 | 3.1130 | S64 | 5.0590 | -0.8975 | 9.0025 |
| S33 | 3.3261 | -3.8635 | 3.1055 | S63 | 3.3457 | -3.8863 | 8.9975 |
| S32 | 0.0050 | -3.8229 | 3.2630 | S62 | -0.0050 | -3.8378 | 9.1800 |
| S31 | -1.6268 | -0.9450 | 3.2855 | S61 | -1.6434 | -0.9661 | 1.6355 |
| S31 | -0.0050 | 1.8814 | 3.2855 | S61 | -0.0150 | 1.9063 | 9.2275 |
| S33 | 1.6828 | 4.8124 | 3.1055 | S63 | 1.6927 | 4.8405 | 8.9975 |
| S33 | -5.0090 | -0.9488 | 3.1055 | S63 | -5.0383 | -0.9544 | 8.9975 |
| S34 | -1.7364 | 4.8145 | 3.1130 | S64 | -1.7523 | 4.8300 | 9.0025 |
| S35 | 1.6769 | -6.7771 | 3.1105 | S65 | 1.6769 | -6.7771 | 8.9975 |
| S34 | -3.3013 | -3.9111 | 3.1130 | S64 | -3.3067 | -3.9325 | 9.0025 |
| S32 | -3.3131 | 1.9071 | 3.2630 | S62 | -3.3211 | 1.9231 | 9.1800 |

Coordinates of atoms within the outermost two trilayers as resulting from the LEED analysis. The z-axis points towards the crystal's bulk. The third trilayer was taken identical to the second one, but laterally shifted by $d = 6.7076$ Å. The vertical distance between atoms S61 and S72 (\equiv S42) was fitted to 2.6195 Å.

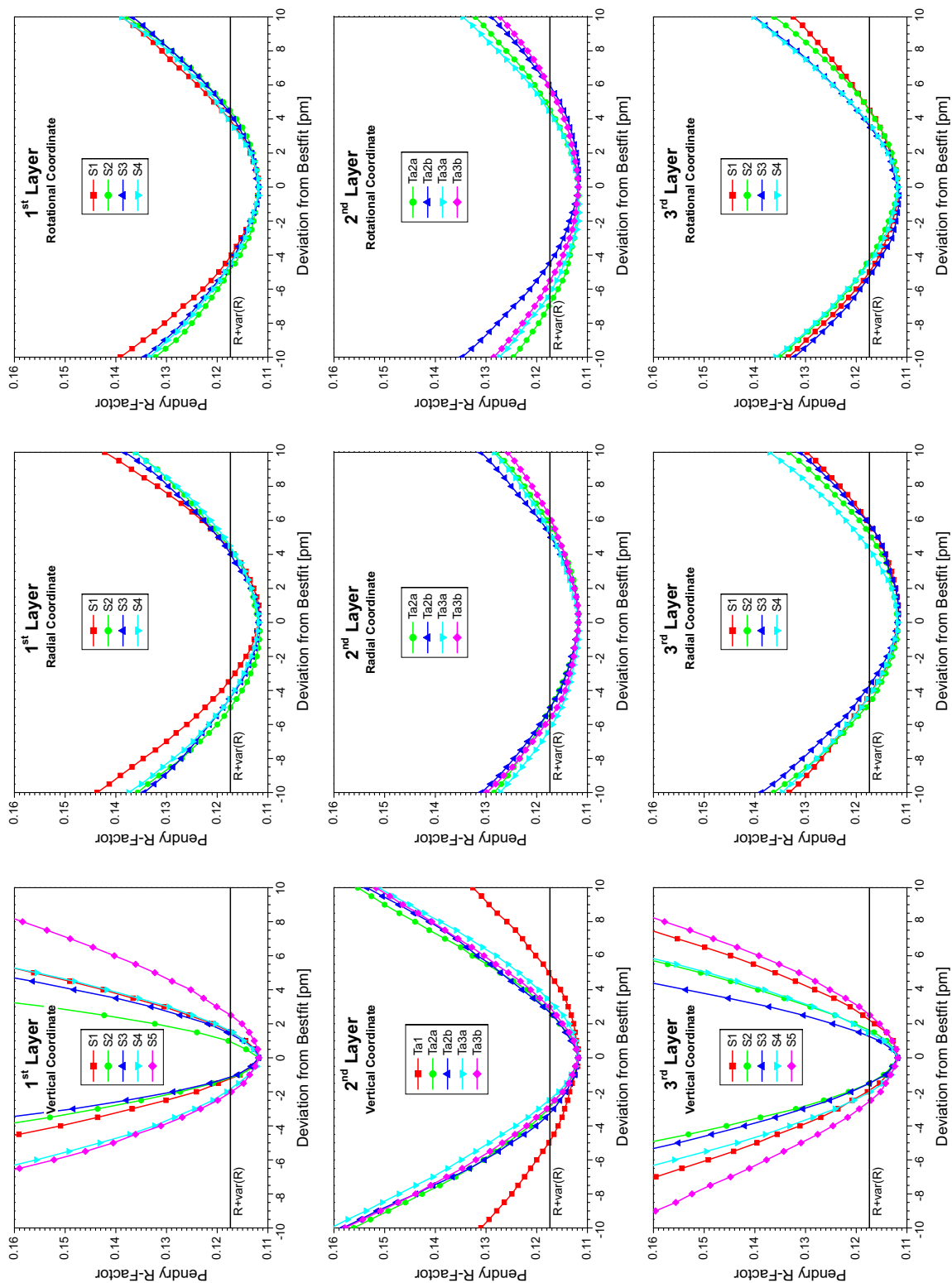
COMPARISON OF EXPERIMENTAL AND CALCULATED BESTFIT SPECTRA

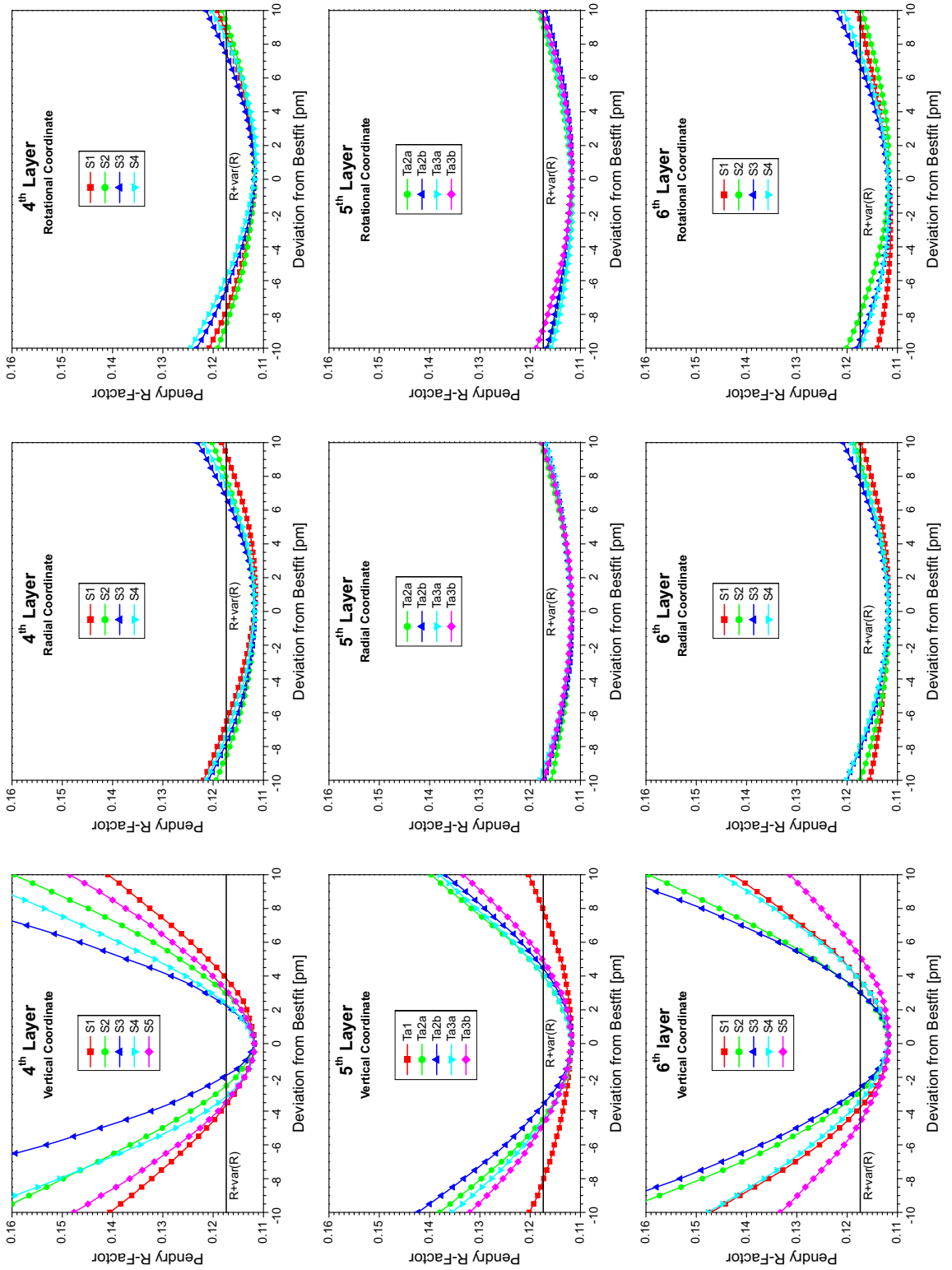




Compilation of all 128 experimental and calculated bestfit spectra entering the LEED-IV analysis. The beam labeling corresponds to the reciprocal mesh of the $(\sqrt{13} \times \sqrt{13})R13.9^\circ$ superstructure.

ERROR CURVES FOR FITTED ATOMIC DISPLACEMENTS





R-factor variation as a function of displacement from the bestfit value (“error curves”) for all site parameters of layers 1 – 6 varied in the analysis. For reasons of computational time saving the error analysis was not performed for azimuthally averaged spectra but for one single azimuth of incidence only ($\Phi = 0$). Therefore, the error curves as well as the variance level are vertically shifted by $\Delta R = 0.002$ compared to the bestfit.